Voxelated 3D Bioprinting Highly Organized Yet Heterogeneous Tissue Constructs

By:
Shannon Grady
Kaylen Kang
Leander Nguyen

University of Virginia, Department of Biomedical Engineering
Spring 2021

Faculty Advisor
Liheng Cai, Ph.D.

Word Count: 4614
Number of Figures: 8
Number of Tables: 0
Number of Equations: 5
Number of Supplements: 1
Number of References: 26

Approved:_____ Date: _____

Li-Heng Cai, Ph.D., Department of Material Science and Engineering, Chemical Engineering and Biomedical Engineering

Voxelated 3D Bioprinting Highly Organized Yet Heterogeneous Tissue Constructs

Shannon P. Grady, [a]Kaylen Y. Kang[a], Leander Q. Nguyen[a], Li-Heng Cai[b,c,d,1], Jinchang Zhu[b]

[a] Fourth Year Biomedical Engineering Undergraduate, University of Virginia
[b] Soft Biomatter Laboratory, Department of Material Science and Engineering, University of Virginia
[c] Department of Chemical Engineering, University of Virginia
[d] Department of Biomedical Engineering, University of Virginia
[1] Correspondence: lc2ta@virginia.edu

Abstract

3D bioprinting utilizes the additive assembly of inks that contain living cells to manufacture tissue mimicking biological constructs. However, one main problem is that current methods of bioprinting utilize 1D filaments as opposed to 0D voxels, the basic building blocks of 3D structures. In this paper, we will introduce a new method that enables microfluidics-assisted digital assembly of spherical particles (DASP). Through this method, the position and size of the hydrogel sphericals can be precisely controlled, thus potentially allowing for the printing of porous 1D lines, 2D arrays, and free-standing 3D lattices. To establish printing parameters for this novel method, our Capstone team characterized the chemical and physical properties of the hydrogel bioink to determine optimal hydrogel hybrid formulations that could effectively print droplets and produce the necessary porosity for nutrient transport. We aimed to characterize and model calcium crosslinking kinetics of the alginate in the hydrogel, diffusion of large biomolecules out of the different bioink formulations, and the effects of poly(ethylene) glycol (PEO) polymer entanglement on mesh size. Our work found the gelation times of alginate hydrogel and determined a model for the diffusion of calcium ions into the alginate hydrogel, determined the feasibility of the diffusion of biomolecules through the hydrogel as well as the effect of alginate concentration on mesh size, and determined how mesh size can be further modulated with the addition of PEO molecules.

Keywords: 3D bioprinting, spherical particle, hydrogel, porosity

Introduction

3D bioprinting involves the layer-by-layer deposition of bioink to fabricate complex constructs that can mimic native tissue, which includes techniques such as inkjet, stereolithography, laser-assisted deposition, and extrusion[1–6]. Of these methods, extrusion-based bioprinting, which consists of depositing thin lines of bioink through a nozzle by mechanical or pneumatic forces, is the most popular for tissue engineering due to its simplicity, affordability, and availability of material[7,8]. However, a major limitation is the distortion of the bioink due to gravity, thus causing a loss of printing fidelity. Several researchers have found success using a bioink with greater viscosities, which provided stronger support against deformation, but at the cost of cell viability[8,9]. This makes it difficult to make cell-friendly and complex 3D structures without the use of sacrificial support.

A modified version of extrusion-based printing, embedded 3D bioprinting, was developed to address these structural challenges by depositing bioink directly into a sacrificial matrix[10,11]. The support matrix with yield-stress behavior allows the print nozzle to move freely in the fluidized support bath and deposit bioink that solidifies as the matrix quickly self-heals[8,10,12]. This overcomes the structural design limitations of printing complex structures with conventional methods since softer bioinks can be extruded in freeform, with increased fidelity, and suspended in the support matrix until the entire structure is crosslinked and mechanically robust[11]. However, this method still utilizes layer-by-layer printing of 1D filaments

or single-step extrusion, which produces bulky and dense structures[12,13]. Although the crosslinked hydrogel allows for the diffusion of small molecules, these constructs don't possess the level of porosity necessary for larger biomolecules to easily diffuse across, thus limiting nutrient transport essential for cellular growth [14]. Therefore, attempts to print larger tissue reconstructs have been limited to organ models that only mimic mechanical properties, not functionality[13].

However, embedded 3D printing technology has recently been used to extrude individual droplets into a support matrix, instead of 1D filaments. A study has observed cytocompatibility of microbes in droplets of growth media for use in small-volume biological assays[15]. However, this model uses oil-based, immiscible fluids to print discrete droplets that are incapable of coalescing into interconnected 3D structures. On the other hand, high density cell clusters, known as spheroids, have shown potential to overcome these limitations through formation of self-assembled organoid structures composed of different cell types[16,17]. Spheroids have been used to create complex tissue structures of the intestine, liver, kidney, brain, and heart for disease model applications *in vitro*[18–22]. A recent study implements a novel assembly technique to bioprint cellular spheroids which are fused to create complex and heterogeneous cardiac microtissue models [6]. This method allows for high spatial organization of two cell types: stem cell-derived cardiomyocytes and cardiac fibroblasts, allowing control of local heterogeneity throughout the construct. However, spheroids must be printed in direct contact with each other and the additional challenge in uniformity of spheroid size means that interparticle distance and porosity cannot be precisely controlled to mimic the highly organized structure of native tissue[23].

We will be introducing a novel 3D printing technique that enables microfluidics-assisted digital assembly of spherical particles (3DASP) to address the shortcomings of these recent developments in 3D bioprinting. To do this, we used the fundamentals behind embedded droplet printing technology to introduce uniformity and control in particle size. Additionally, depositing cell-encapsulated hydrogel particles directly into a support matrix will allow for the formation of interconnected droplets at varying interparticle distances that can coalesce by swelling and crosslinking. This direct control and augmentation of particle size and neighboring distances would produce the porosity and heterogeneity necessary to engineer more viable tissue reconstructs.

To provide additional context and background information on the 3DASP bioprinting method, **Supplemental Figure 1** has been included in the Supplemental Material. In summary, DASP works by first depositing bio-ink droplets of customizable size at a precise location in a supporting matrix. The bio-ink is a mixture of cells and a solution consisting of two polymers, alginate and poly(ethylene oxide) (PEO). The supporting matrix is a suspension of gelatin microparticles and contains calcium ions. Once the droplets are printed, they swell to coalesce with one another. In the meantime, calcium ions in the supporting matrix diffuse into the bio-ink droplet to partially crosslink the alginate.

Following complete crosslinking of the alginate network and subsequent removal of the sacrificial supporting matrix, the printed droplets form a 3D lattice of interconnected yet distinguishable hydrogel particles.

For our Capstone project, we mainly focused on characterizing the ideal physical and chemical properties of the hydrogel that would be required for the potential bioprinting of pancreatic islets. This included determining the time it takes for the alginate hydrogel to crosslink, modeling the time it takes for dextran to release from the hydrogel, and modeling how the entanglements of the PEO molecules affect the mesh size of the hydrogel.

Results

Alginate Hydrogel Crosslinking Time:

Due to covid, Jinchang, the graduate student in Dr. Cai's lab performed the crosslinking kinetics for us. We hypothesized that increasing the calcium concentration would decrease the gelation time. Using a stress controlled rheometer, he measured the real time viscoelasticity of the alginate hydrogel at varying concentrations of calcium. As seen in **Figure 1** he quantified the gelation time(T_g) of the hydrogel by determining the time it took for the storage modulus G' to become larger than the loss modulus G".

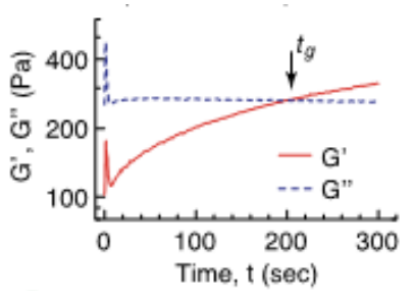

Fig. 1. Gelation and crosslinking kinetics of the supporting gelatin matrix. Using a stress-controlled rheometer, the gelation time was calculated by determining the time it takes for the storage modulus G' to become larger than the loss modulus G".

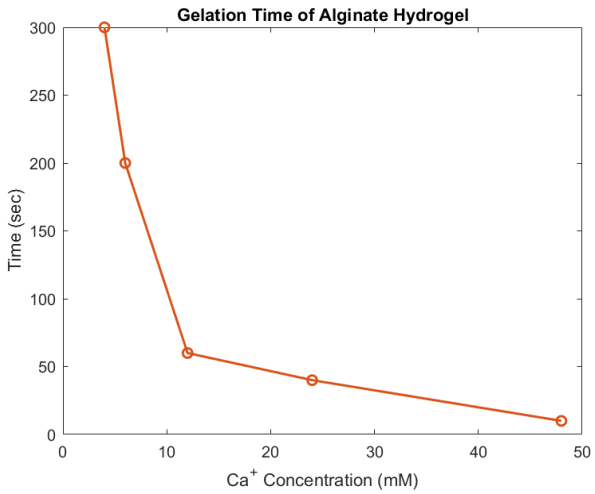

Fig. 2. Crosslinking kinetics of gelatin matrix at varying concentrations of calcium. Using a stress-controlled rheometer, the gelation time was calculated by determining the time it takes for the storage modulus G' to become larger than the loss modulus G''.

The gelation times for varying concentrations of calcium were calculated using the method described above, which can be seen in figure 2. The gelation time decreases by nearly 30 times from 300 to 10 seconds as the Ca2+ concentration increases from 3 to 48 mM, thus validating our original hypothesis.

Model of Calcium Diffusion

To explain these results, we used ficks second law of diffusion to model the gelation time (**Eq. 1 & 2**).

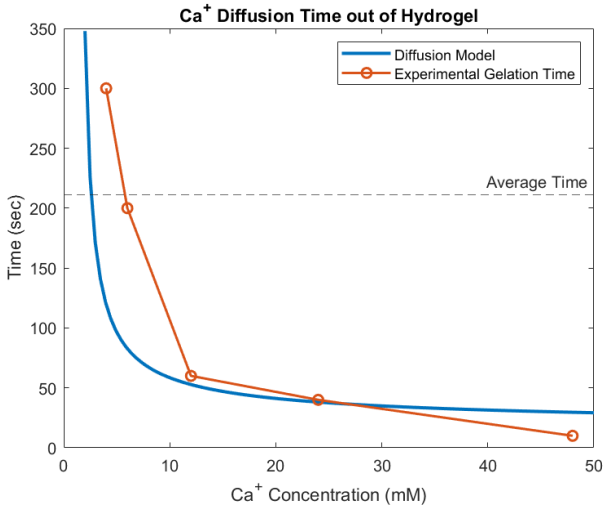

Fig. 3. Modeling the calcium diffusion into the alginate hydrogel. Based on the theoretical distance the calcium molecule would have to diffuse to crosslink hydrogel a droplet (1 mm) and the diffusion coefficient of calcium in an aqueous solution (0.79 X$10^{-5} cm^2/2$), Fick's second law of diffusion was used to model and explain the experimental gelation times collected by Jinchang.

As seen by the graph in **Figure 3,** our model (blue line) resembles the experimental data collected by Jinchang. Depending on the crosslinking agent, size, and overall complexity of the construct in the future, these equations can be used to determine the ideal concentration and the corresponding gelation time needed.

$$\frac{d_c}{d_t} = D\left(\frac{d^2C}{dx^2}\right) \quad [1]$$

$$\frac{C_x}{C_s} = 1 - erf\left(\frac{x}{2*\sqrt{D*T}}\right) \quad [2]$$

Dextran Release Profile from Alginate Hydrogel

Once crosslinking kinetics were characterized to create an optimal bioink, the graduate student conducted experiments to characterize biomolecule release profiles. Dextran is slightly larger than many important biomolecules including insulin which is why it was chosen for the experiments. Fluorescently-labeled 70 kDa dextran was used to represent a large biomolecule and release profiles were characterized using intensity from microscopy images. Microscopy was used to measure intensity over time and the results are shown in **Figure 4a**. Significant differences between $Alg_{1.5}$ (**red, Figure 4b**) and $Alg_{4.0}$ (**blue, Figure 4b**) formulations were observed, meaning it takes longer for dextran to diffuse in $Alg_{4.0}$. We determined that this was due to the smaller mesh size of this hydrogel formulation.

However, the addition of PEO molecules to the $Alg_{1.5}$ formulation did not result in major differences in diffusion time for dextran (**green, Figure 4b**). This result provides evidence that the mesh size of the bioink hydrogel is determined by the concentration of the crosslinked alginate and not so much by the uncrosslinked PEO molecules, although it does play a role in bio-ink viscoelasticity which will be discussed in the following sections.

As mentioned, the chemically crosslinked alginate is the main determinant of the mesh size of the hydrogel bio-ink. It is important to understand the microscale porosity of the hydrogel because it must allow for free diffusion of biomolecules, including nutrients to support cell viability and free PEO molecules that will diffuse out of the construct over time. An optimal mesh size must allow for diffusion without compromising the structural integrity of the construct.

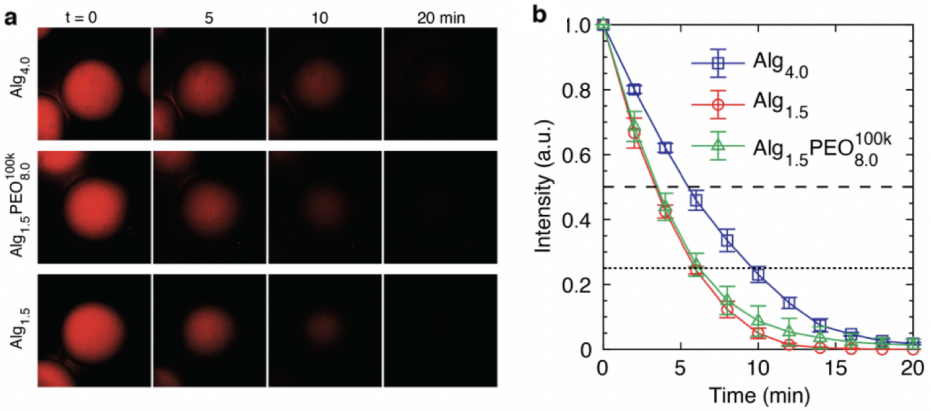

Figure 4: Characterization of dextran release from alginate hydrogel. (a) Fluorescence microscopy images of dextran release from alginate 4.0%, alginate 1.5% with PEO, and alginate 1.5%, from t = 1 to t = 20 minutes. **(b)** Intensity vs. time for alginate 1.5% represented by the red line, alginate 4.0% represented by the blue line, and alginate 1.5% with PEO represented by the green line.

Model of Dextran Release from Alginate Hydrogel

To model these results, we identified a model to characterize the diffusion of biomolecules within the construct. The obstruction-scaling model of solute diffusion was used because it provides a model for the effects of the alginate polymer mesh size and solute size on the diffusivity. We found an exponential increase in diffusivity with an increase in mesh size. This makes sense because particles have more space to diffuse when there is less crosslinked polymer in the way. The equation for the obstruction-scaling model is below (**Eq. 2**) and a graphical representation of the model is shown in **Figure 5**. In this model, D_0 is the diffusion coefficient of the solute in water, D_g is the diffusion coefficient of the solute in the hydrogel, r_f is the radius of the polymer chain, R is the radius of the solute probe, and ξ is the distance between polymer crosslinks[24,25]. To model the experiments done by the graduate student, a value of R=2.5nm was used for 70kDa dextran, r_f = 0.83nm for alginate, and r_f = 0.23nm for PEO. The correlation length, ξ, relates to the average mesh size of the network, with $\xi = 13nm$ for pure $Alg_{1.5}$, $\xi = 9\ nm$ for $Alg_{1.5}PEO_{8.0}^{100k}$, and $\xi = 6nm$ for $Alg_{4.0}$.

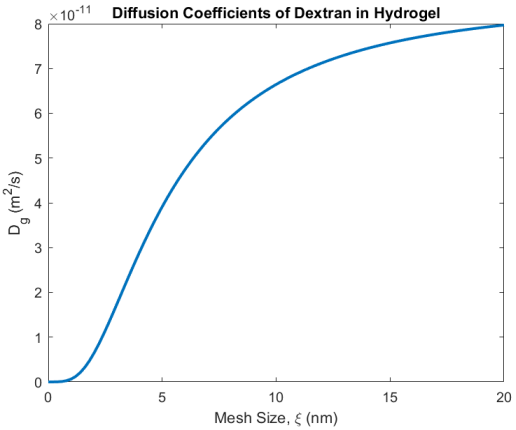

Figure 5: Obstruction-scaling model for solute diffusion in a hydrogel. Exponential increase in diffusion coefficient is seen as mesh size increases.

$$D_g = D_o exp[-\ \pi(\frac{R+r_f}{\xi+2r_f})^2] \qquad [3]$$

Using the model the diffusion coefficients, D_g, was calculated to be 7.30e-11 m^2/s for $Alg_{1.5}$ and for 4.74e-11 m^2/s for $Alg_{4.0}$.

To determine the experimental rate of diffusion, D_g was found using the time it took for dextran to completely diffuse out of the hydrogel droplet (**Eq. 3**). This is quantified by the time at which the intensity reached zero. For $Alg_{1.5}$, this time was t = 16 minutes and for $Alg_{4.0}$, it was t = 20 minutes.

$$t = \frac{r^2}{6D_g} \qquad [4]$$

r is the radius of the hydrogel droplet (r = 0.05mm) and D_g is the diffusion coefficient of the solute in the hydrogel. Diffusion coefficients of D = 8.68e-11 m^2/s and D = 6.94e-11 m^2/s were found for $Alg_{1.5}$ and $Alg_{4.0}$, respectively.

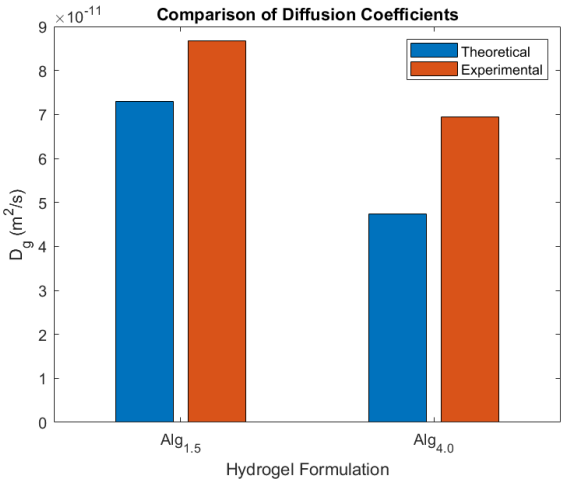

Figure 6: Comparison of experimental and theoretical data for dextran release in alginate hydrogel. Comparison of model (blue) to experiment (orange) diffusion coefficients for dextran in alginate hydrogel. Percent error of 18.9% was observed in the alginate 1.5% while a 46.4% percent error was observed in the 4.0% alginate composition.

Next, we compared diffusion coefficients for experimental (**orange, Figure 6**) to model (**blue, Figure 6**). The comparison suggested that the model matches well with the experimental data, however a limitation is that only one set of data was used. The percent errors between the theoretical and experimental diffusion coefficient values for $Alg_{1.5}$ and $Alg_{4.0}$ were 18.9% and 46.4%, respectively. More experimentation is needed with a greater range of alginate concentrations to determine the goodness of fit for the model. In theory, this model can be extrapolated to different biomolecules of various sizes to determine diffusivity within a hydrogel construct.

PEO Polymer Entanglement

The PEO molecules were originally added to the hydrogel bioink formulation to increase viscosity and improve fidelity of the individual hydrogel droplets when they are initially printed. As only the alginate is chemically crosslinked, the PEO polymers eventually become free molecules and diffuse out of the hydrogel. However, with the results of the dextran experiment, changes to the mesh size of the alginate hydrogel were observed and warranted further investigation. We hypothesized that this was due to polymer chains becoming entangled and trapped in the alginate mesh longer than the probe time. To determine the effect of the PEO polymers on the porosity of the hydrogel, the mesh size of different hydrogel formulations with varying molecular weights of PEO polymers were quantified by observing the shear storage modulus, G. The shear storage moduli were measured using a stress-controlled rheometer with hydrogel bioink formulations containing 1.5% (w/v) alginate and PEO polymers with molecular weights of 100K, 300K, and 1000K (**Figure 7a**).

A formulation of 4.0% (w/v) alginate was used as an additional control. Using the network modulus equation with shear modulus G, Boltzmann's constant and temperature (**Eq. 4**), the mesh sizes of the hydrogel bioink formulations for $Alg_{1.5}$, $Alg_{1.5}PEO_{8.0}^{100K}$, $Alg_{1.5}PEO_{6.9}^{300K}$, $Alg_{1.5}PEO_{3.5}^{1000K}$, and $Alg_{4.0}$ were estimated to be 13 nm, 12 nm, 11 nm, 9 nm, and 6 nm, respectively (**Figure 7b**).

$$\xi = -(k_B T/G)^{1/3} \quad [5]$$

The shear-controlled rheometric measurements proved that PEO polymers did have a linear effect on the mesh size of the hydrogel. It was hypothesized that this was due to the entanglement of the PEO polymers forming

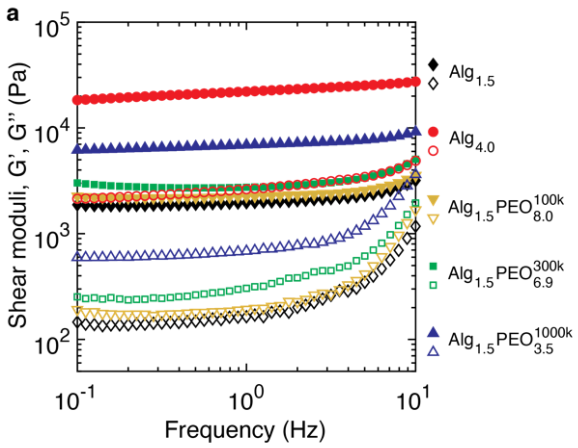

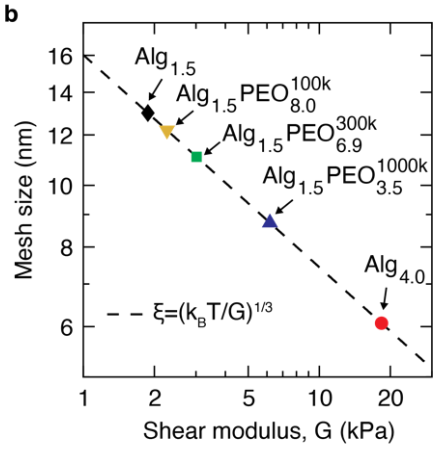

Figure 7: Characterization of the porosity of the bioink hydrogel particles. (a) The shear moduli were measured for the varying types of bioink formulation using a rheometer with an oscillatory frequency of 0.1 to 10 Hz. The filled symbols represent the storage modulus G' and the unfilled symbols represent the loss modulus G". **(b)** The estimated mesh sizes of the different hydrogels calculated from the storage modulus and compared to display the wide range of control when adding PEO molecules.

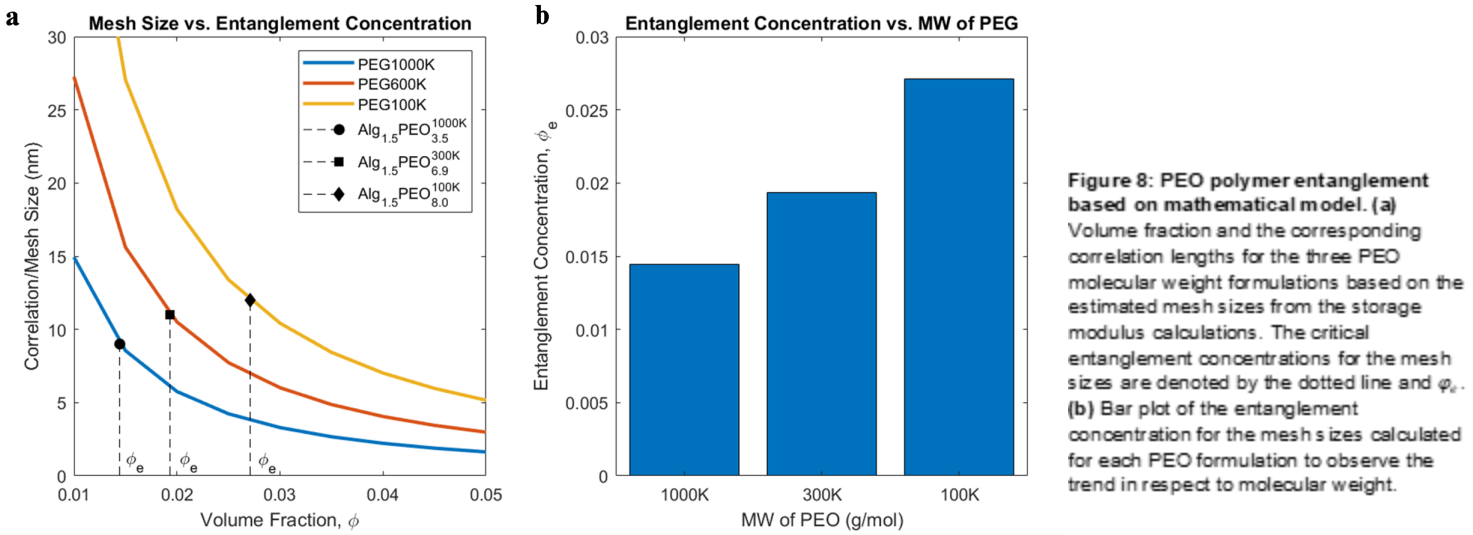

Figure 8: PEO polymer entanglement based on mathematical model. (a) Volume fraction and the corresponding correlation lengths for the three PEO molecular weight formulations based on the estimated mesh sizes from the storage modulus calculations. The critical entanglement concentrations for the mesh sizes are denoted by the dotted line and φ_e. **(b)** Bar plot of the entanglement concentration for the mesh sizes calculated for each PEO formulation to observe the trend in respect to molecular weight.

physical cross linkers that prevented the free movement of the polymers. This entanglement thereby created an additional mesh network that could possibly hinder the diffusion of other biomolecules. As higher molecular weight PEO polymers were made of longer chains, these larger polymers stayed entangled longer and stayed trapped in the hydrogel for a longer period of time.

Model of PEO Polymer Entanglement

To provide a more mathematically robust explanation for this decrease in mesh size with respect to increased molecular weight of PEO, a model was derived using entanglement concentration, φ_e, and correlation size, ξ, assuming an athermal, or good, solvent (**Eq. 5**). The $a(1)$ represents the tube diameter of the PEO polymer, which was found to be 4 nm[26]. Additionally, the Nvalue represents the number of Kuhn's monomers, which we simplified to represent the number of monomers on a polymer chain.

$$\xi = \varphi_e^{-11/8} \frac{a(1)}{\sqrt{N}} \qquad [6]$$

Since correlation size is synonymous with mesh size and the number of monomers on a PEO polymer chain, N, is directly related to its molecular weight by the equation MW = 44.05N +18.02, this model provides the mathematical relationship between mesh size entanglement concentration, and the effect that molecular weight has on these values.

Using the three experimental PEO polymer molecular weights, the critical volume fraction for entanglement was plotted using the mesh size calculated from the shear moduli measurements, where $Alg_{1.5},PEO_{8.0}{}^{100K}$, $Alg_{1.5},PEO_{6.9}{}^{300K}$, and $Alg_{1.5},PEO_{3.5}{}^{1000K}$ had entanglement concentrations of 0.0271, 0.0193, and 0.0144, respectively (**Figure 8a**). This showed that a lower volume fraction was needed to reach the critical concentration at which the polymers entangled to form physical crosslinkers in higher molecular weight PEO compared to lower molecular weight PEO. This corresponds to greater entanglement of PEO polymers of higher molecular weight within the volume of solution in the hydrogel.

To observe the relationship between entanglement concentration and molecular weight of the experimental PEO polymers shown in the equation, their corresponding values were plotted in a bar graph (**Figure 8b**).

Once the experimental data was plugged into the mathematical models we derived, the relationship was clear between the effects of longer chains on entanglement concentration and mesh size. The higher molecular weight PEO had on average smaller mesh sizes over the possible volume fraction concentrations. Additionally, the mesh sizes that were observed in the experiment correlated to entanglement concentrations that were aligned with the hypothesis. It took higher molecular weight PEO to reach a critical concentration of polymers within a volume to begin to entangle. This shows that higher molecular weight PEO is much more effective at entangling with one another than lower molecular weight PEO since this is able to occur at lower concentrations.

Discussion

Determining the crosslinking kinetics for individual droplets is crucial in ensuring the balance between droplet solidification and printing speed. The crosslinking kinetics needs to be carefully controlled so that the printed droplets can coalesce before solidifying. We determined that the optimal calcium concentration for the 3DASP pancreatic islet sacrificial supporting matrix was 6mM, which was associated with a gelation time of 200 seconds. With a printing speed of one second, hundreds of droplets can be printed before solidifying, thus allowing for the interconnecting and coalescing between all of them.

Modeling this crosslinking process is also important because depending on the crosslinking agent, size, and overall complexity of the construct in the future, different gelation times will be needed. The ideal calcium concentration and gelation time mentioned in the previous paragraph were designed for working with pancreatic islets from mice. One limitation with this model is that it assumes that the calcium molecules diffuse in 1D, when in reality it diffuses in 3D manner. This can create inaccuracies and may be one of the possible reasons why our model doesn't follow the experimental data exactly. Another limitation is that there may be other processes besides Fick's laws of diffusion.

Modeling the diffusion kinetics of the hydrogel bio-ink is important because it allows for characterization of biomolecule diffusion throughout the construct. The obstruction-scaling model of solute diffusion can be extrapolated to biomolecules of different sizes by modulating the parameters to reflect those of said biomolecule. Since it was determined that alginate crosslinking plays the most important role in determining mesh size, polymer concentration can be modulated to obtain a desired level of diffusion. It is important to understand the microscale porosity of the hydrogel because it must allow for free diffusion of biomolecules, including nutrients to support cell viability and free PEO molecules that will diffuse out of the construct over time. An optimal mesh size must allow for diffusion without compromising the structural integrity of the construct.

Dextran, being similar in molecular weight to insulin, was particularly of interest to this project since pancreatic islets are currently the primary application of the novel DASP printing method. A limitation, however, is that dextran was the only molecule for which diffusion kinetics were examined and characterized. Other biomolecules, such as glucagon, should be tested in order to further assess the feasibility of diffusion throughout the 3D construct.

As we previously thought that the addition of PEO polymers would act on viscosity and be independent of mesh size, it was important to further investigate the slight differences in mesh size that was observed during the dextran experiment. The addition of PEO polymers did improve fidelity, printing more spherical droplets with the use of a more biocompatible 1.5% alginate, instead of 4.0% alginate. The $Alg_{4.0}$ formulation produced mesh sizes too small for efficient diffusion of biomolecules and transport of nutrients, so the addition of PEO polymers were supposed to increase the viscosity without decreasing the mesh size. Though the results did show that there was a relationship between higher molecular weight PEO and smaller mesh sizes, these mesh sizes were still large enough for biomolecules, 5 nm as a reference, to diffuse through.

Overall, the experiment and mathematical model determined that the addition of PEO polymers can further fine-tune the mesh size of the hydrogel, which will be useful to modulate for different tissue types in the future. Although the PEO polymers are expected to eventually disentangle and become free molecules that diffuse out of the hydrogel, the transport of nutrients in the early stages of cellular growth in the hydrogel scaffold, before it is washed away, is critical to the viability of the tissue. It is important to maintain a good balance of increased viscosity for printing fidelity without significantly compromising the porosity of the hydrogel bioink that is important for nutrient transport, which this model will prove useful in determining.

Limitations of the model include the accuracy of the polymer tube diameter, $a(1)$, and number of Kuhn's monomers, N. These are theoretical values that we did not measure ourselves, and were either found in literature or indirectly calculated. However, this does not skew the general trend that was observed when using the model. Also, this model describes a small volume segment of the hydrogel, which we used to make conclusions about the entire bulk hydrogel solution, assuming uniformity and homogeneity throughout the hydrogel.

Conclusion

In conclusion, the results from this paper provide a proof-of-concept of our new bioprinting method (3DASP). By being able to precisely control the crosslinking kinetics, by either increasing or decreasing the amount of calcium, the neighboring hydrogel droplets will be able to interconnect, thus potentially being able to form a highly

complex 3D lattice structure. The model created from Fick's second law can be used in the future depending on the overall complexity of the construct.

The results from characterizing and modeling the release of dextran from alginate, show that diffusion of relevant biomolecules is also feasible. The level of porosity and mesh size can be controlled mainly through the concentration of alginate used, which is important as the porosity of hydrogel particles determine its ability to exchange nutrients and other relevant molecules. Although the level of porosity is mainly determined by the concentration of alginate, the addition of PEO molecules can further modulate the effective network mesh size in the range of 9 to 12 nm, due to entanglements being trapped in the alginate network. However, the PEO molecules are not chemically bound to the alginate, thus eventually escaping over time.

With the use of these models, and other factors such as a viscosity and loss factor, optimal printing parameters for the hydrogel bioink droplets can be determined for specific tissue and cell types, such as the pancreatic islet that was printed at the lab. This will allow for the highly organization needed for tissue constructs, as well as augmentations throughout the printing process to introduce heterogeneity in construct.

Some future directions include experimentation with a variety of other bioinks other than alginate and PEO to test whether 3DASP is still able to successfully print highly porous and heterogeneous constructs. In addition, with the models that were created, other tissue constructs besides pancreatic islets can be considered by modulating the printing parameters and bioink formulations. Overall, 3DADP provides a method for creating highly organized yet heterogeneous tissue constructs.

Materials and Methods

Materials

Gelatin from porcine skin (gel strength 300, Type A, Cat. No. G2500), alginic acid sodium salt from brown algae (medium viscosity, Cat. No. A2033), poly(ethylene oxide) (PEO) with MW of 5000, 1000, 300, 100 kDa (Cat. No. 189472, 182001, 372781, 181986), and poly(ethylene glycol) (PEG) with MW of 35 kDa (Cat. No.81310) were all purchased from Sigma-Aldrich (USA). Fluorescent labeling reagents including EDC (Cat. No. E7750), Sulfo-NHS (Cat. No. 56485) and fluoresceinamine (Cat. No. 201626) were purchased from Sigma-Aldrich (USA). Fluorescently labeled dextran (Texas RedTM, MW=70,000 Da, ex 595/em 615, Cat. No. D1830) was purchased from Fisher Scientific (USA).

Hardware: 3D Motion System

A 3D motion system was built by replacing the hotmelt extruder of a desktop printer (JGURORA z-603s) with a custom made extrusion module. The extrusion model was built based on a linear screw (T8) actuator which converts the rotary motion of a stepper motor (NEMA 17) into linear motion. The microfluidic model was built using a micropipette puller (P‑1000, Sutter Instrument, Inc.) to taper a cylindrical glass capillary (World Precision Instruments, Inc.) of inner and outer diameters 0.58 mm and 1.00 mm, respectively, to a diameter of 20 μm and then was carefully sanded to a final diameter of 60 μm.

Preparation of the Alginate Bioink and Gelatin supporting matrix

To prepare the gelatin supporting matrix, the gelatin was dissolved in a calcium solution (6 mM calcium chloride, 30 mM sodium chloride) with a concentration of 1.5% w/v at a temperature of 50 ℃. The solution was then cooled at 4 ℃ for 12 hours to form the hydrogel. 200 mL of the hydrogel is then mixed with 30 mL calcium solution and fragmented into microparticles using a blender operated at 4000 rpm for 100 sec to create a matrix consisting of jammed gelatin microparticles. This results in a supporting matrix that is mechanically yield-stress fluid, and can self-heal in less than a second

To create the alginate bioink, alginic acid sodium salt was dissolved in DI water at 4% w/v. The mixture was then sonicated for 2 hours at 60 ℃ to make a homogenous solution.

Rheological Characterization

To perform the rheological measurements, a stress-controlled rheometer (Anton Paar, MCR 302) with 25 mm plate-plate geometry at 20℃ was used. To characterize the stress yield behavior of the supporting matrix, we conduct a stress sweep from 0.1 to 1000 Pa at an oscillatory frequency of 1 Hz. To determine the gelation time of alginate bioink, we monitor in real-time the and at an oscillatory shear frequency of 1 Hz and a shear strain of 1%. We choose a gap size of 1 mm, comparable to the dimension of a printed droplet.

Dextran Release

To characterize the bio-ink mesh size, we dissolve the fluorescently labeled dextran at a concentration of 2 mg/mL in the bio-ink. The bio-ink droplet was then placed into a crosslinking solution, DI water with 50 mM Ca2+ to solidify the particle. The particle is then

immediately transferred into DMEM (without glucose, glutamine, phenol red, and sodium pyruvate) and then incubated for 30 min to fully equilibrate with the medium. We then replace the washing medium by a fresh DMEM medium that contains no dextran, during which the fluorescence of the particle is monitored using confocal laser scanning fluorescence microscopy (Leica SP8). The half-decay time of the fluorescence intensity is then used to assess the mesh size of the hydrogel particle.

Mathematical Modeling

Equations and concepts used for the derivation of the polymer entanglement equation were found in the textbook *Polymer Physics* by Michael Rubenstein and Ralph H. Colby[26]. The model was derived with the following equations found in literature: $\xi = b\varphi^{-v/(3v-1)}$, $\varphi_e = [\frac{N_e(1)}{N}]^{4/5}$, and $N_e(1) = (\frac{a(1)}{b})^2$, where the polymer is an athermal solvent, with a v = 3/5. All mathematical modelling was conducted using MATLAB 2019a (MathWorks) software. Experimental data was plugged into various models and data visualization tools on MATLAB were coded to plot and display results.

End Matter

Author Contributions and Notes

L.H.C, J.Z, S.P.G, K.Y.K., and L.Q.N. designed research, J.Z. performed research, S.P.G, K.Y.K., and L.Q.N. analyzed data; and S.P.G, K.Y.K., and L.Q.N. wrote the paper.

The authors declare no conflict of interest.

Acknowledgments

We would like to thank Professor Liheng Cai, PhD and graduate student, Jinchang Zhu, from the Soft Biomatter Laboratory at the University of Virginia Department of Material Sciences Engineering, Chemical Engineering, and Biomedical Engineering for advising us through this project this past year.

References

1. Bishop, E. S. *et al.* 3-D bioprinting technologies in tissue engineering and regenerative medicine: Current and future trends. *Genes & Diseases* **4**, 185–195 (2017).

2. Boland, T., Xu, T., Damon, B. & Cui, X. Application of inkjet printing to tissue engineering. *Biotechnology Journal* **1**, 910–917 (2006).

3. Dey, M. & Ozbolat, I. T. 3D bioprinting of cells, tissues and organs. *Scientific Reports* **10**, 14023 (2020).

4. Khademhosseini, A., Langer, R., Borenstein, J. & Vacanti, J. P. Microscale technologies for tissue engineering and biology. *PNAS* **103**, 2480–2487 (2006).

5. Murphy, S. V. & Atala, A. 3D bioprinting of tissues and organs. *Nature Biotechnology* **32**, 773–785 (2014).

6. Ozbolat, I. T. & Hospodiuk, M. Current advances and future perspectives in extrusion-based bioprinting. *Biomaterials* **76**, 321–343 (2016).

7. Ning, L. & Chen, X. A brief review of extrusion-based tissue scaffold bio-printing. *Biotechnology Journal* **12**, 1600671 (2017).

8. Shiwarski, D. J., Hudson, A. R., Tashman, J. W. & Feinberg, A. W. Emergence of FRESH 3D printing as a platform for advanced tissue biofabrication. *APL Bioengineering* **5**, 010904 (2021).

9. Ribeiro, A. *et al.* Assessing bioink shape fidelity to aid material development in 3D bioprinting. *Biofabrication* **10**, 014102 (2017).

10. Bhattacharjee, T. *et al.* Writing in the granular gel medium. *Science Advances* **1**, e1500655 (2015).

11. Wu, W., DeConinck, A. & Lewis, J. A. Omnidirectional Printing of 3D Microvascular Networks. *Advanced Materials* **23**, H178–H183 (2011).

12. Kolesky, D. B. *et al.* 3D Bioprinting of Vascularized, Heterogeneous Cell-Laden Tissue Constructs. *Advanced Materials* **26**, 3124–3130 (2014).

13. Mirdamadi, E., Tashman, J. W., Shiwarski, D. J., Palchesko, R. N. & Feinberg, A. W. FRESH 3D Bioprinting a Full-Size Model of the Human Heart. *ACS Biomater. Sci. Eng.* **6**, 6453–6459 (2020).

14. Compaan, A. M., Song, K., Chai, W. & Huang, Y. Cross-Linkable Microgel Composite Matrix Bath for Embedded Bioprinting of Perfusable Tissue Constructs and Sculpting of Solid Objects. *ACS Appl. Mater. Interfaces* **12**, 7855–7868 (2020).

15. Nelson, A. Z., Kundukad, B., Wong, W. K., Khan, S. A. & Doyle, P. S. Embedded droplet printing in yield-stress fluids. *PNAS* **117**, 5671–5679 (2020).

16. Daly, A. C., Davidson, M. D. & Burdick, J. A. 3D bioprinting of high cell-density heterogeneous tissue

models through spheroid fusion within self-healing hydrogels. *Nature Communications* **12**, 753 (2021).

17. Lancaster, M. A. & Knoblich, J. A. Organogenesis in a dish: Modeling development and disease using organoid technologies. *Science* **345**, (2014).

18. Broutier, L. *et al.* Culture and establishment of self-renewing human and mouse adult liver and pancreas 3D organoids and their genetic manipulation. *Nat Protoc* **11**, 1724–1743 (2016).

19. Cruz-Acuña, R. *et al.* Synthetic hydrogels for human intestinal organoid generation and colonic wound repair. *Nature Cell Biology* **19**, 1326–1335 (2017).

20. Lancaster, M. A. *et al.* Cerebral organoids model human brain development and microcephaly. *Nature* **501**, 373–379 (2013).

21. Richards, D. J. *et al.* Human cardiac organoids for the modelling of myocardial infarction and drug cardiotoxicity. *Nature Biomedical Engineering* **4**, 446–462 (2020).

22. Takasato, M. *et al.* Kidney organoids from human iPS cells contain multiple lineages and model human nephrogenesis. *Nature* **526**, 564–568 (2015).

23. Fang, Y. & Eglen, R. M. Three-Dimensional Cell Cultures in Drug Discovery and Development. *SLAS DISCOVERY: Advancing the Science of Drug Discovery* **22**, 456–472 (2017).

24. Amsden, B. An Obstruction-Scaling Model for Diffusion in Homogeneous Hydrogels. *Macromolecules* **32**, 874–879 (1999).

25. Hadjiev, N. A. & Amsden, B. G. An assessment of the ability of the obstruction-scaling model to estimate solute diffusion coefficients in hydrogels. *Journal of Controlled Release* **199**, 10–16 (2015).

26. Rubenstein, M. & Ralph, C. *Polymer Physics*. (OUP Oxford, 2003).

Supplemental Material

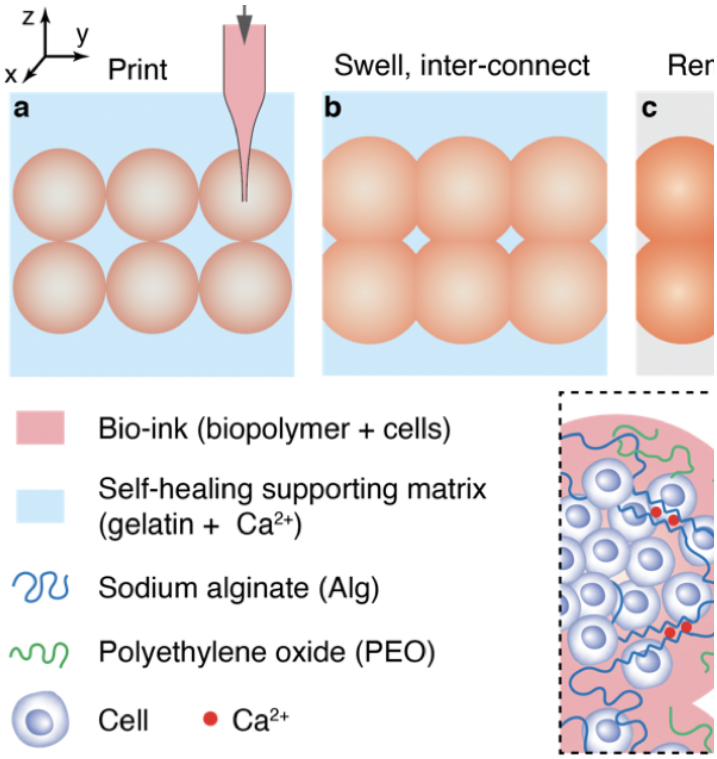

Supplemental Fig. 1: An overview of the 3DASP bioprinting method including bio-ink and supporting matrix components. Bioink consists of alginate and PEO molecules while the supporting matrix contains gelatin and calcium ions.